

## Insights into the structural complexity and local disorder of crystalline AsTe<sub>3</sub> from Semi-Automated First-Principles Modelling

Sylvian Cadars,<sup>\*a</sup> Olivier Masson,<sup>a</sup> Jean-Paul Laval,<sup>a</sup> Firas E. Shuaib,<sup>a</sup> Andrea Piarristeguy,<sup>b</sup> Gaëlle Delaizir<sup>a</sup> and Assil Bouzid<sup>a</sup>

### ELECTRONIC SUPPLEMENTARY INFORMATION

#### Electronic Supplementary Information (ESI) content:

Figure S1: Rietveld refinement of experimental XRD data using a  $1 \times 8 \times 1$  supercell of elemental Te.

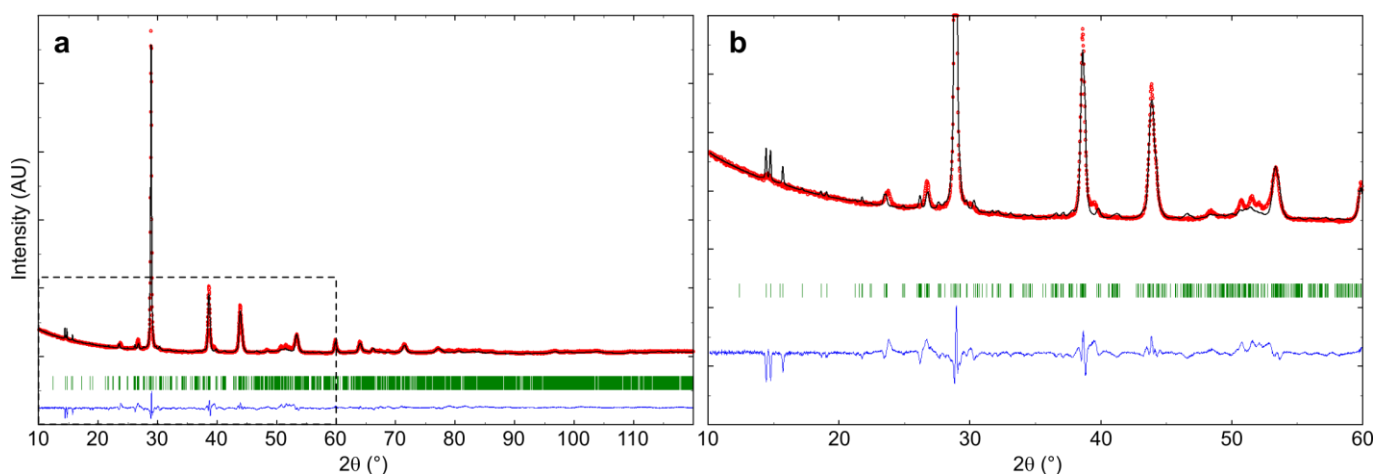
Figure S2: Combined refinement of experimental X-ray diffraction and total scattering data using a  $1 \times 8 \times 1$  supercell of elemental Te.  
Figure S3: Detailed results of calculations conducted using different exchange and correlation functionals and van der Waals corrections.

Figure S4: Representations of additional model structures among the ten with best global score.

Figure S5: Comparisons of X-ray total scattering data measured experimentally for AsTe<sub>3</sub> glass and crystal and for  $\alpha$ - and  $\beta$ -As<sub>2</sub>Te<sub>3</sub>

Figure S6: PDF data simulated from FPMD at 300 K and in the course of simulated annealing runs.

Figure S7: Graphical representations of the paths between high-symmetry k-points sampling the Brillouin zones for band-structure calculations.



**FIGURE S1.** Experimental X-ray diffractogram (red circles) of crystalline AsTe<sub>3</sub>, Rietveld refinement (black line) using a  $1 \times 8 \times 1$  supercell of elemental Te (originally in the P3<sub>1</sub>21 space group and converted to P1 for the supercell model), and difference thereof (in blue). (a) Main peaks in the 20–80 ° range. (b) Magnification of Low-intensity peaks in the 10–60° range. Reflexions predicted from the refined model are shown as green vertical lines. The  $B_{\text{iso}}$  values were fixed at 0.5 Å<sup>2</sup> for all atoms, the shape of the line profile was modelled by a Pseudo-Voigt with a constant FWHM of 0.16°  $2\theta$  and a mixing parameter of 0.6. A total of 76 parameters were refined, with the final atomic positions deviating reasonably from the starting positions (mean and maximum displacements of 0.4 Å and 0.7 Å respectively). As mentioned in the main text, the purpose of this Rietveld refinement is to validate an initial supercell hypothesis to serve as a basis for the construction of our models, rather than for the final evaluation of a structure.

<sup>a</sup> Institut de Recherche sur les Céramiques (IRCER), UMR CNRS 7315-Université de Limoges, France.

<sup>b</sup> ICGM, Univ Montpellier, CNRS, ENSCM, Montpellier, France

\* Corresponding author: sylvian.cadars@unlim.fr

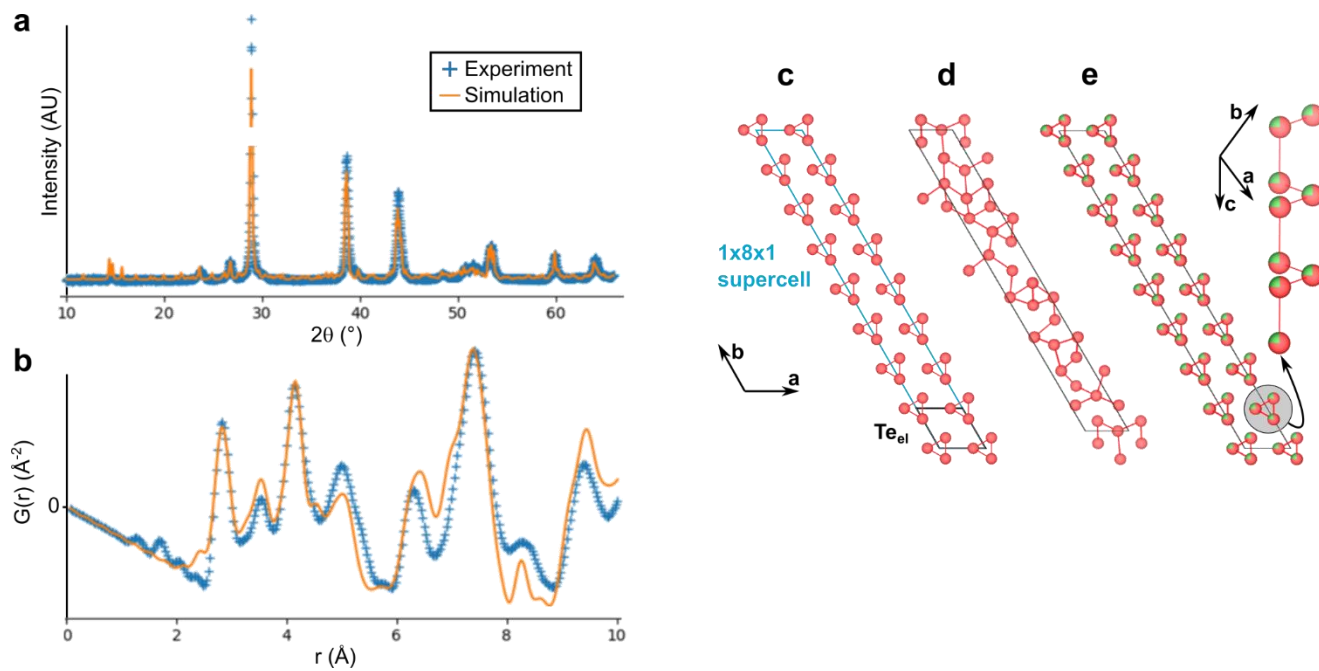


**FIGURE S2.** (a, b) Experimental (blue crosses) X-ray (a) diffraction and (b) total scattering data collected for crystalline  $AsTe_3$ , and simulated data (orange line) obtained by combined refinement of these data, with a pure-Te model (in d) obtained with a 1x8x1 supercell of elemental Te (in c) as the starting point. (e) 1x8x1 supercell derived from  $Te_{el}$ , modified with 25%:75% As:Te mixed composition on all sites.

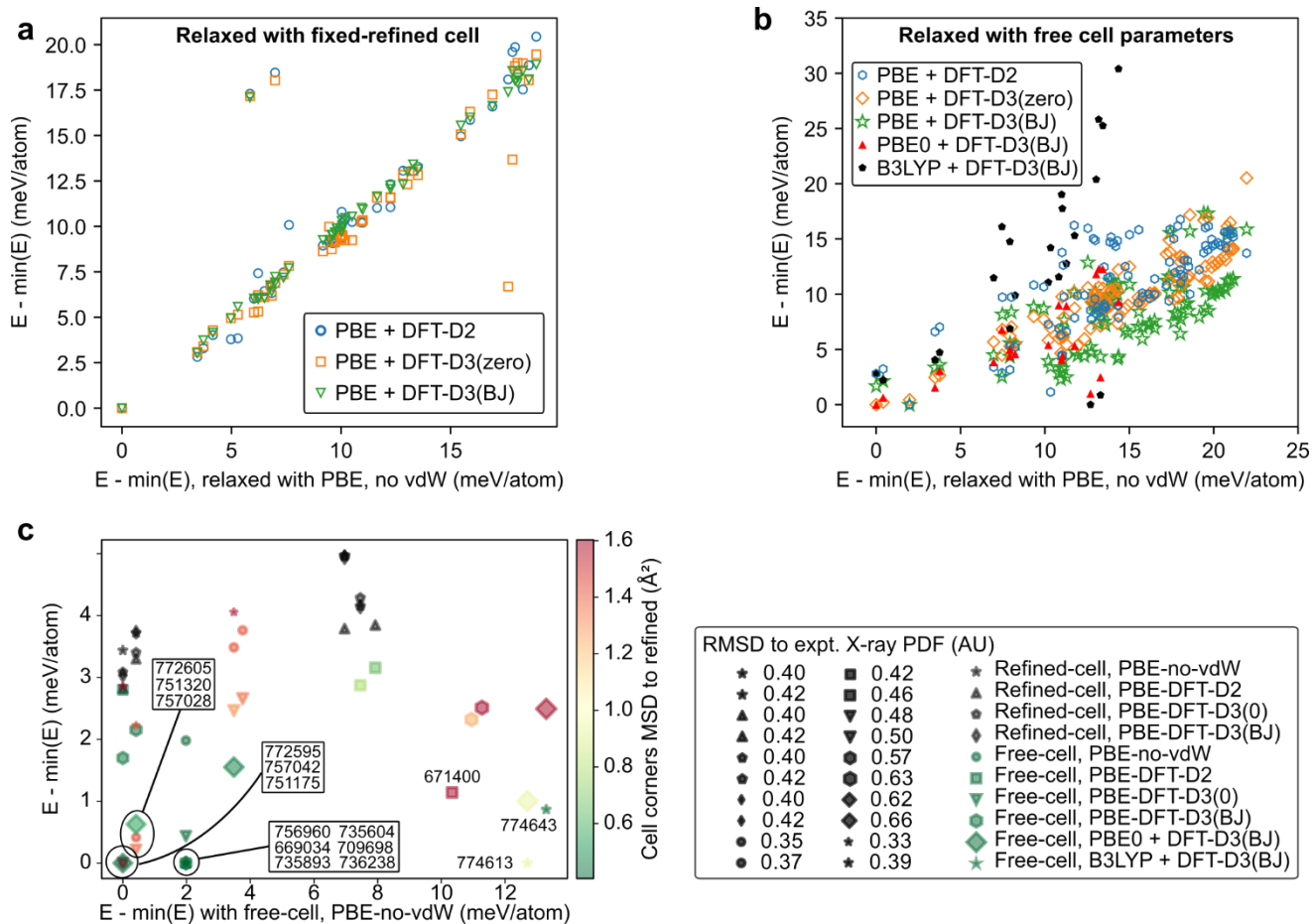


**FIGURE S3.** Comparisons of DFT energies obtained after relaxation with different functionals, with and without different van der Waals correction schemes, and cell parameters (a) fixed or (b) relaxed. In every case the final energy after relaxation with the considered setting is plotted as a function of the energy of the same structure relaxed with a “reference setting” corresponding to the PBE functional and no van der Waals correction applied. In (c) we also examine agreements to experimental unit-cell parameters (symbol colours, for free-cell relaxations) and PDF data (symbol sizes). See legend to the right to relate the sizes of the different symbols with the  $RMSD_{PDF}(i, k)$  calculated for the considered  $As/Te$  configuration  $i$  relaxed with the considered DFT setting  $k$ . Black symbols indicate structures relaxed with fixed-refined-cell parameters.

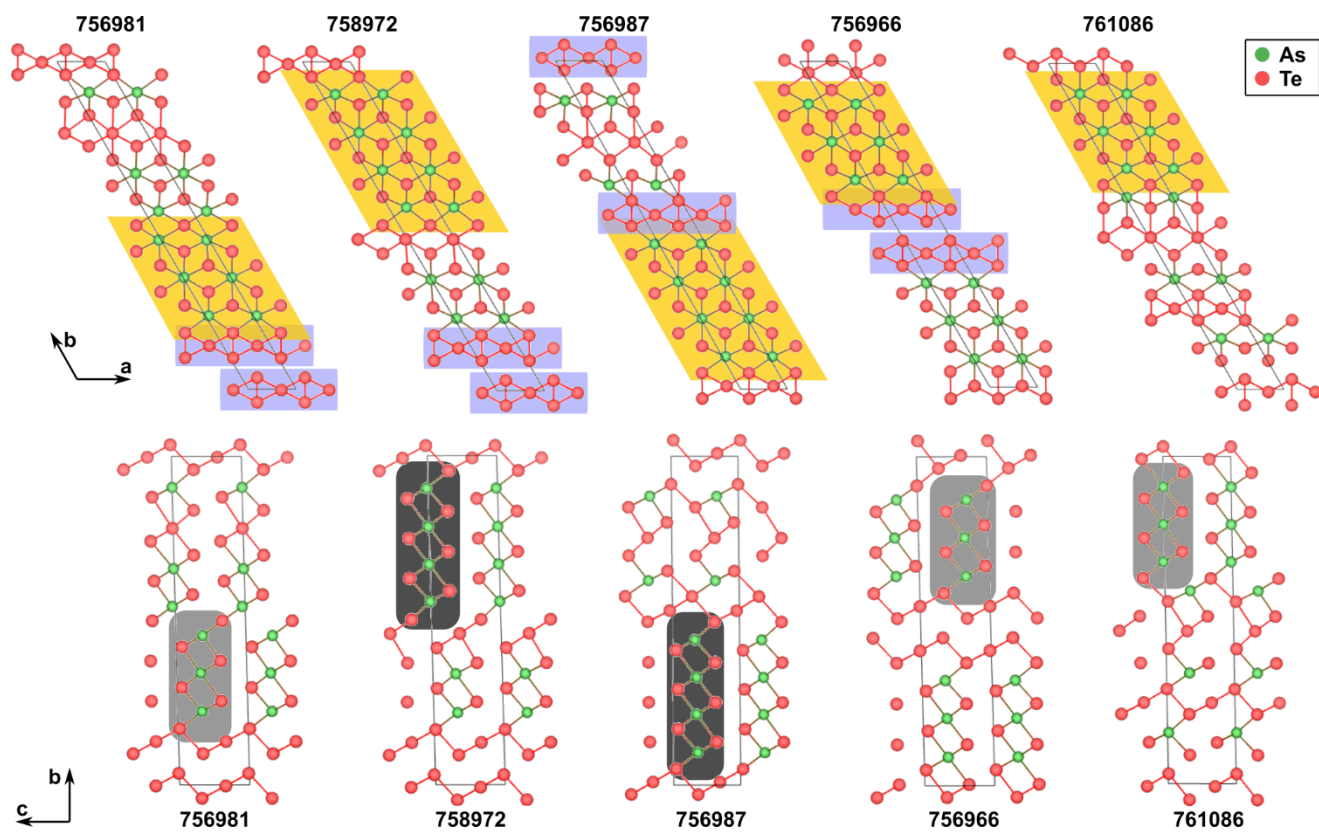


**FIGURE S4.** Visualizations of some representative structures among the ten with best global score, with the exception of the first and second, which are shown in the manuscript Figure 3. Views are along (top) the c crystallographic axis and (bottom) the b crystallographic axis.

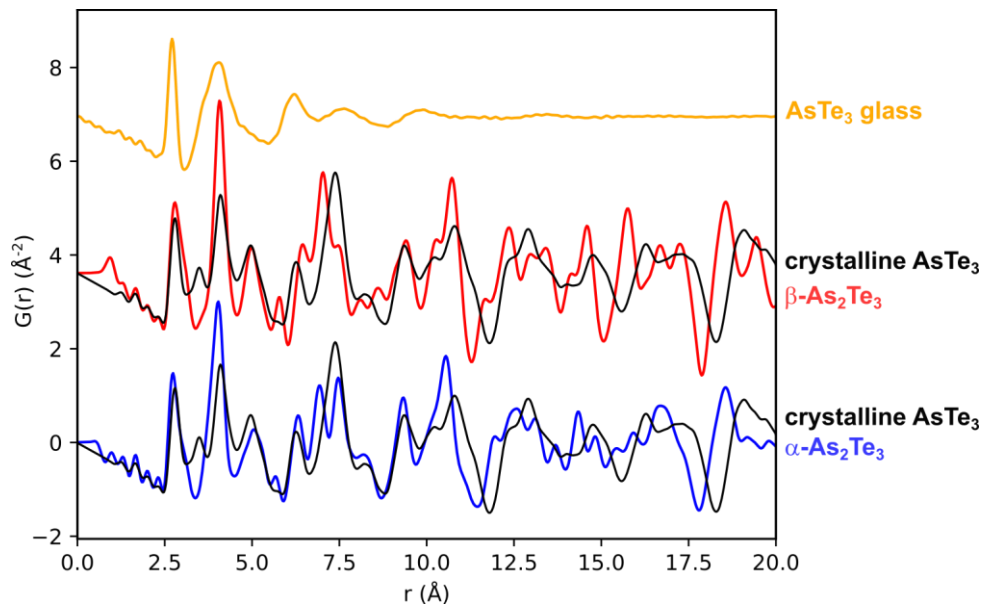


**FIGURE S5.** Comparison of experimental PDF data collected for crystalline AsTe<sub>3</sub> (in black), amorphous AsTe<sub>3</sub> (in gold),  $\alpha$ -As<sub>2</sub>Te<sub>3</sub> (in blue) and  $\beta$ -As<sub>2</sub>Te<sub>3</sub> (in red) up to  $r = 20 \text{ \AA}$ .

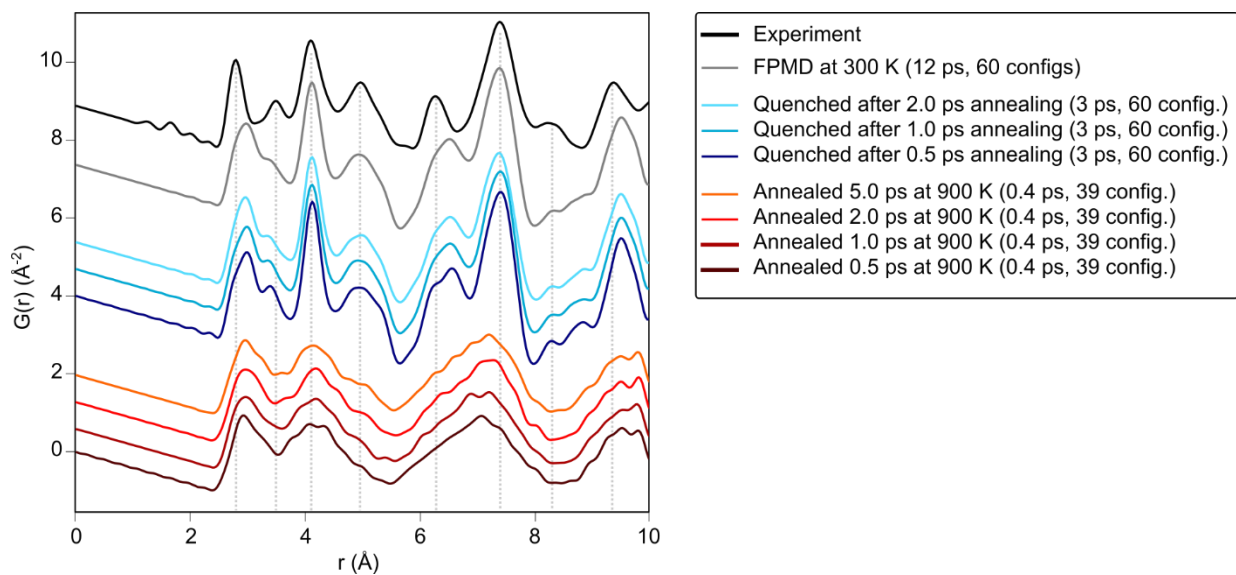


**FIGURE S6.** Simulated X-ray total scattering PDFs obtained in the course of this 900 K annealing phase by averaging over a duration of 0.4 ps are shown in brown to orange colours. PDF data obtained after a fast quenching (600 K for 3 ps and 300 K for 1 ps) at different times of the annealing phase are shown in blue, and compared to the PDF obtained from a room-temperature FPMD in gray, and the experimental PDF in black.

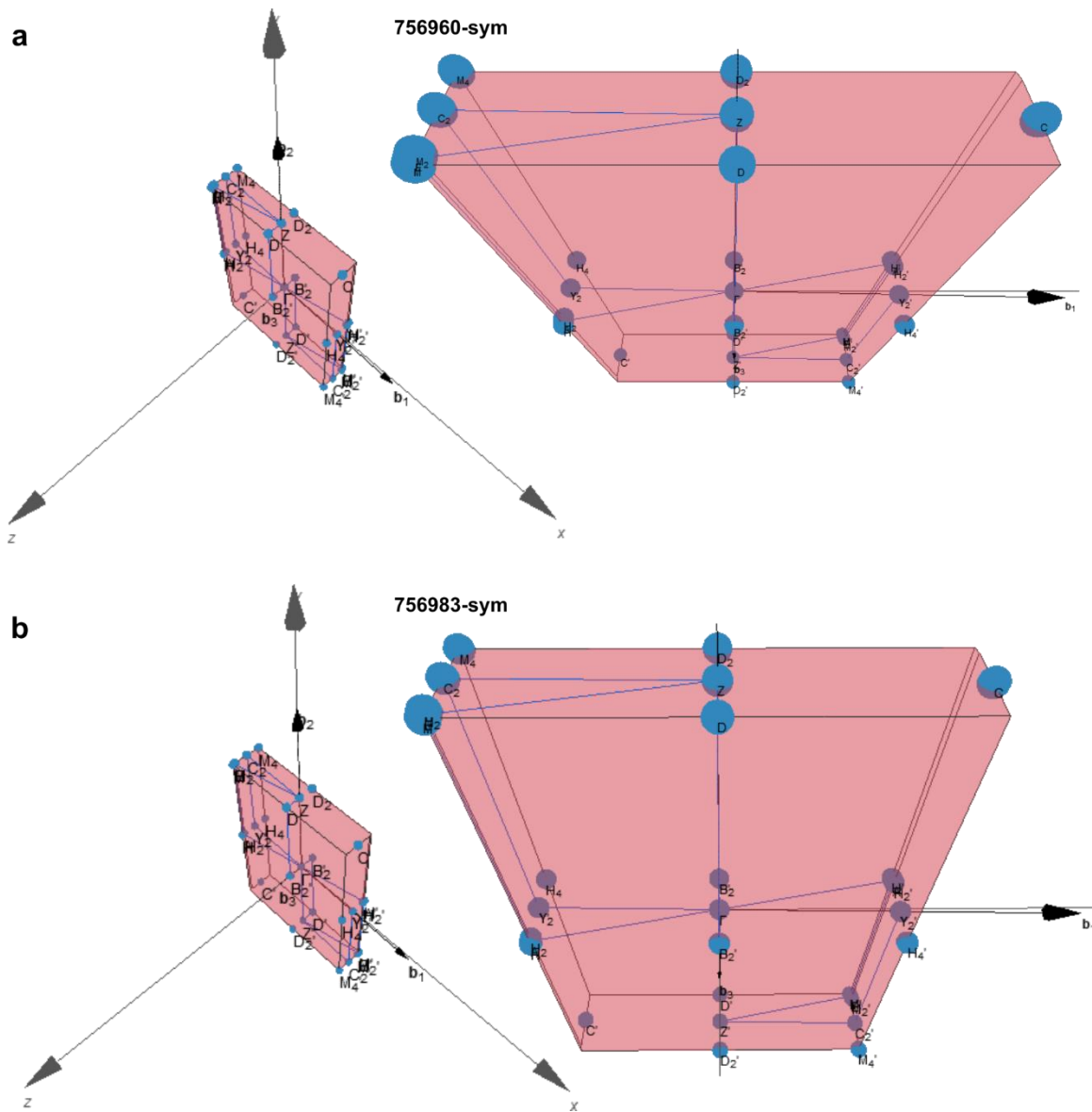


**FIGURE S7.** Graphical representations of the k-point paths used to sample the Brillouin zone for the calculation of the band structures of  $\text{AsTe}_3$  models (a) 756960-sym and (b) 756983-sym discussed in the manuscript Figure 8. The “SeeK-path: the k-path finder and visualizer” page hosted within Materials Cloud was used for visualization (<https://tools.materialscloud.org/seekpath/>). See Refs <sup>54,55</sup> in manuscript.